14. Boss, A. P. & Durisen, R. H. in *Chondrites and the Protoplanetary Disk* (eds Krot, A. N., Scott, E. R. D. & Reipurth, B.) (Astrophysical Society of the Pacific, in the press).
15. Wood, J. A. On the formation of meteoritic chondrules by aerodynamic drag heating in the solar nebula. *Earth Planet. Sci. Lett.* 70, 11–26 (1984).
16. Boss, A. P. & Graham, J. A. Clumpy disk accretion and chondrule formation. *Icarus* 106, 168–178 (1993).
17. Weidenschilling, S. J., Marzari, F. & Hood, L. L. The origin of chondrules and jovian resonances. *Science* 279, 681–684 (1998).
18. Wood, J. A. Processing of chondritic and planetary materials in spiral density waves in the nebula. *Meteorit. Planet. Sci.* 31, 641–645 (1996).
19. Nakamoto, T., Hayashi, M. R., Kita, N. T. & Tachibana, S. in *Chondrites and the Protoplanetary Disk* (eds Krot, A. N., Scott, E. R. D. & Reipurth, B.) (Astrophysical Society of the Pacific, in the press).
20. Weisberg, M. K. et al. A new metal-rich chondrite group. *Meteorit. Planet. Sci.* 36, 401–418 (2001).
21. Petaev, M. I., Meibom, A., Krot, A. N., Wood, J. A. & Keil, K. The condensation origin of zoned metal grains in Queen Alexandra Range 94411: implications for the formation of the Bencubbin-like chondrites. *Meteorit. Planet. Sci.* 36, 93–106 (2001).
22. Campbell, A. J., Humayun, M., Meibom, A. J., Krot, A. N. & Keil, K. Origin of zoned metal grains in the QUE94411 chondrite. *Geochim. Cosmochim. Acta* 65, 163–180 (2001).
23. Alexander, C. M. O'D. & Hewins, R. H. Mass fractionation of Fe and Ni isotopes in metal in Hammadah al Hamra 237. *Meteorit. Planet. Sci.* 39, A13 (2004).
24. Campbell, A. J., Humayun, M. & Weisberg, M. K. Siderophile element constraints on the formation of metal in the metal-rich chondrites Bencubbin, Weatherford, and Gujba. *Geochim. Cosmochim. Acta* 66, 647–660 (2002).
25. Kleine, T., Mezger, K., Palme, H., Scherer, E. & Münker, C. Early core formation in asteroids and late accretion of chondrite parent bodies: Evidence from ¹⁸²Hf-¹⁸²W in CAIs, metal-rich chondrites and iron meteorites. *Geochim. Cosmochim. Acta* (submitted).
26. Melosh, H. J., Cassen, P., Sears, D. & Lugmair, G. in *Workshop on Chondrites and the Protoplanetary Disk* (eds Krot, A. N., Reipurth, B. & Scott, E. R. D.) 125–126 (Hawaii Institute of Geophysics and Planetology, School of Ocean and Earth Science and Technology, University of Hawaii at Manoa, Honolulu, 2004).
27. Wetherill, G. W. & Stewart, G. Formation of planetary embryos: effects of fragmentation, low relative velocity, and independent variation of eccentricity and inclination. *Icarus* 106, 190–209 (1993).
28. Chambers, J. E. & Cassen, P. The effects of nebula surface density profile and giant-planet eccentricities on planetary accretion in the inner solar system. *Meteorit. Planet. Sci.* 37, 1523–1540 (2002).
29. Kleine, T., Mezger, K. & Palme, H. The Hf-W age of the lunar magma ocean. *Lunar Planet. Sci.* XXXVI, 1940 (2005).
30. Canup, R. M. Simulations of a late lunar-forming impact. *Icarus* 168, 433–456 (2004).

LETTERS

Experimental measurement of the photonic properties of icosahedral quasicrystals

Weining Man[1,2], Mischa Megens[3], Paul J. Steinhardt[1] & P. M. Chaikin[1,2,4]

Quasicrystalline structures may have optical bandgap properties—frequency ranges in which the propagation of light is forbidden—that make them well-suited to the scientific and technological applications for which photonic crystals[1–3] are normally considered[4]. Such quasicrystals can be constructed from two or more types of dielectric material arranged in a quasiperiodic pattern whose rotational symmetry is forbidden for periodic crystals (such as five-fold symmetry in the plane and icosahedral symmetry in three dimensions). Because quasicrystals have higher point group symmetry than ordinary crystals, their gap centre frequencies are closer and the gaps widths are more uniform—optimal conditions for forming a complete bandgap that is more closely spherically symmetric. Although previous studies have focused on one-dimensional and two-dimensional quasicrystals[4–7], where exact (one-dimensional) or approximate (two-dimensional) band structures can be calculated numerically, analogous calculations for the three-dimensional case are computationally challenging and have not yet been performed. Here we circumvent the computational problem by doing an experiment. Using stereolithography, we construct a photonic quasicrystal with centimetre-scale cells and perform microwave transmission measurements. We show that three-dimensional icosahedral quasicrystals exhibit sizeable stop gaps and, despite their quasiperiodicity, yield uncomplicated spectra that allow us to experimentally determine the faces of their effective Brillouin zones. Our studies confirm that they are excellent candidates for photonic bandgap materials.

In 1984, Schechtman *et al.* observed icosahedral symmetry with five-fold rotation axes in the electron diffraction pattern of an alloy of Al-Mn (ref. 8). Simultaneously, the concept of long range quasiperiodic order with icosahedral symmetry was theoretically developed by Levine and Steinhardt[9,10]. Our realization of a photonic icosahedral quasicrystal is shown in Fig. 1a. The diamond structure in Fig. 1b was made for comparative experiments; diamond has been suggested as an optimal structure for photonic crystals.

Photonic crystals are based on the fact that photons Bragg-scatter from a medium with a periodically modulated refractive index. Multiple scattering at frequencies near the Bragg condition prevents propagation in these directions, producing a 'stop gap'. Overlap of the stop gaps in all directions yields a complete photonic bandgap and traps the light. Intuitively, the complete overlap occurs more readily in more isotropic structures. Quasicrystals have long-range quasiperiodic order and higher point group symmetries, so photons Bragg-scatter along a more spherically symmetric set of directions. Many recent papers address this question in two dimensions[4,6,7]. As the symmetry increases, the Brillouin zone becomes more circular or more spherical. Photonic quasicrystals also allow for a higher degree of flexibility and tunability for defect mode properties[5].

Figure 1c shows the effective Brillouin zone (related to the pseudo-Jones zone used in describing electronic transport in quasicrystals[11,12]) of the icosahedral structure with its irreducible Brillouin zone highlighted in yellow. For comparison, Fig. 1d shows the first Brillouin zone of the diamond (face-centred cubic, f.c.c.) structure with its irreducible Brillouin zone. Note that, as a measure of sphericity, along the edge of the diamond structure's irreducible Brillouin zone the magnitude of **k** (which is proportional to the stop gap centre frequency to a first-order approximation) increases 29.1% from L to W. Along the edge of the effective irreducible triacontahedral Brillouin zone of the icosahedral structure, the magnitude of **k** increases only 17.5% from the two-fold to the five-fold symmetry points. Moreover the triacontahedron's faces are identical and subtend smaller solid angles.

A *D*-dimensional periodic lattice has *D* independent basis vectors, whereas $D + N$ linearly independent vectors (with integer $N \geq 1$
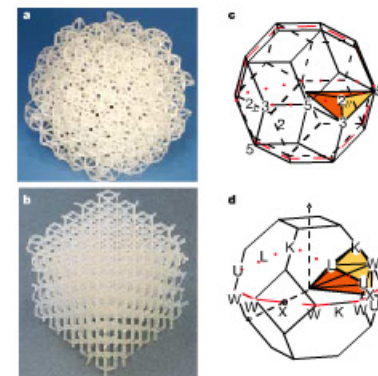

Figure 1 | Experimental photonic structures and their Brillouin zones.
a, Stereolithographically produced icosahedral quasicrystal with 1-cm-long rods. **b**, Diamond structure with 1-cm-long rods. **c**, Triacontahedron, one of several possible effective Brillouin zones with icosahedral symmetry. **d**, Brillouin zone for the f.c.c./diamond structure.

[1]Department of Physics, [2]Princeton Institute for the Science and Technology of Materials, Princeton University, Princeton, New Jersey, 08544, USA. [3]Philips Research Laboratories, Prof. Holstlaan 4, NL-5656 AA Eindhoven, The Netherlands. [4]Department of Physics and Center for Soft Condensed Matter Research, New York University, New York 10003, USA.
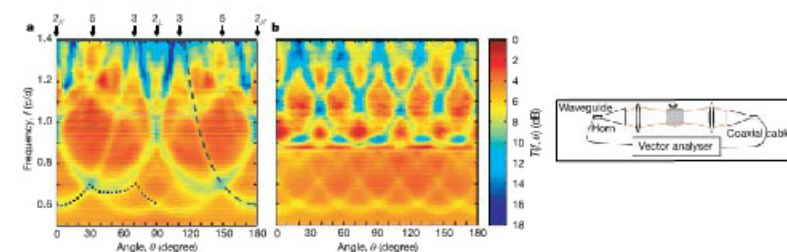
Figure 2 | Measured transmission for an icosahedral quasicrystal. a, $T(f,\theta)$, transmission as a function of frequency (measured in units of c/d) and angle, for a rotation about a two-fold rotation axis of the quasicrystal (corresponding to the dotted line in Fig. 1c) using two overlapping frequency bands. The dashed line is a $1/\cos\theta$ curve characteristic of Bragg scattering from a Brillouin zone face. **b,** $T(f,\theta)$ for a rotation about a five-fold rotation axis corresponding to the dashed line in Fig. 1c. Inset, schematic of the microwave horn and lens arrangement used for these measurements.

Figure 3 | Comparison of calculated bands and measured transmission for a diamond structure. a, Calculated dispersion relation f on the boundary of the first Brillouin zone versus θ, for the diamond structure along the dotted curve in Fig. 1d. **b,** $T(f,\theta)$ for the sample rotation along the same curve. There is excellent agreement at the photonic gap centre frequencies.
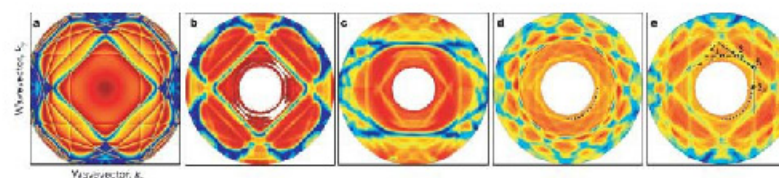
Figure 4 | Imaging of Brillouin zone for diamond and icosahedral quasicrystal structures. a, Brillouin zone for the diamond structure along the four-fold direction as seen in the contour plot of calculated frequency deviation $(\delta f = f - (c/\bar{n})|\mathbf{k}|/(2\pi))$ versus k. **b–e,** The Brillouin zone can be seen in a plot of the measured $T(r = f, \theta = \theta)$ (using the same scale as Fig. 3) for the diamond lattice along the four-fold (dashed in Fig. 1d) axis (**b**) and two-fold (dotted in Fig. 1d) axis (**c**); and for the quasicrystal along the five-fold (dashed in Fig. 1c) and two-fold (dotted in Fig. 1c) axes (**d**). The inner decagon in **d** and the solid and dashed lines in **e** correspond to the dashed and dotted lines in Fig. 1c. The dash-dotted line is a non-triacontahedral zone face.

and D an integer) are required to describe the quasicrystal lattice. The icosahedral quasicrystal lattice of points can be constructed by projecting the points of a six-dimensional hypercubic lattice, the six-dimensional analogue of a three-dimensional cubic lattice. The coordinate of any lattice point can be described by the relation: $R = \sum_{i=1}^{6} n_i \mathbf{a}_i$, where the n_i are a subset of the integers and $\mathbf{a}_i$ are the six basis vectors: $\mathbf{a}_1 = (1,\tau,0)$, $\mathbf{a}_2 = (-1,\tau,0)$, $\mathbf{a}_3 = (0,1,\tau)$, $\mathbf{a}_4 = (0,-1,\tau)$, $\mathbf{a}_5 = (\tau,0,1)$, $\mathbf{a}_6 = (\tau,0,-1)$, and $\tau = (\sqrt{5}-1)/2$, the golden mean. The structure has twelve five-fold, fifteen three-fold and thirty two-fold symmetry axes. We generate the lattice points of the icosahedral structure and create a solid structure by using equal length rods to connect points in pairs. We have made the overall shape a dodecahedron, so that each of the 12 outside faces will be perpendicular to a five-fold rotation axis, as shown in Fig. 1a.

Our crystals were created with a stereolithography machine (model SLA-250 from 3D Systems) that produces a solid plastic model by ultraviolet laser photopolymerization. The resolution is 0.1 mm lateral and 0.15 mm vertical. Both of our crystals have vertices connected with rods, of length $d = \sqrt{3}a/4 = 1$ cm. The rod diameter is 0.15 cm for our quasicrystal and 0.4 cm for the diamond structure. Our quasicrystal has 694 cells, 4,000 rods, and consists of 17.3 vol.% polymer. Our diamond structure has 500 cells and is 7.36% polymer. We measured the refractive index $\bar{n}$ of the polymerized SLA5170 resin by placing a solid block in a waveguide and recording the transmission and reflection spectrum. For 33-GHz microwaves ($\lambda = 0.91$ cm in air), $\bar{n} = 1.65 - 0.025i$. The resulting $(1/e)$ absorption length is 12 wavelengths. (The index absorption from the polymer reduces the transmission approximately as $\exp(-2\omega\eta L/c)$, where $\eta = 0.025$ is the imaginary part of the refractive index and L is the transmission path length. The actual attenuation will depend on the geometry and the modes. In all curves in Figs 2–4 we have multiplied by the same simple exponential factor to reduce the background slope. This has no effect on the gap determination.)

Transmission measurements were made with a HP Model 8510C Vector Analyser in three bands, from 8 to 15, from 15 to 26 and from 26 to 42 GHz. To approximate plane waves, a single TE_{10} mode was coupled through two sets of horn-attached waveguides with two custom-made polystyrene microwave lenses as schematically shown in the inset in Fig. 2. Before the sample was inserted, the transmission spectrum of the set-up is recorded for normalization. The sample has different symmetry and dimensions in different directions, so the transmission spectrum should be sensitive to orientation and polarization. The sample was aligned so that the incident beam was perpendicular to one of the sample's rotational symmetry axes. We rotated the sample along that rotational symmetry axis, and recorded the relative transmission spectrum every 2 degrees. For the quasicrystal, a rotation about the two-fold axis covers all the external
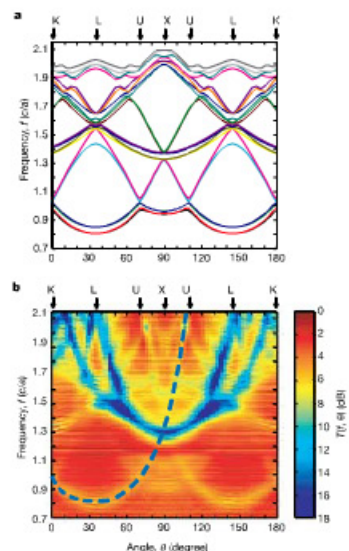
points of the irreducible Brillouin zone and both polarizations. The region covered by the rotation about the two-fold (or five-fold) axis is shown as the dotted (dashed) red line in Fig. 1c. In Fig. 2 we show the measured transmission $T(f,\theta)$ for this rotation in overlapping plots from two frequency bands.

The simplest way to check our entire procedure is to perform the experiments on our diamond structure, where we are able to make a direct comparison with calculated stop gaps. We obtain the photonic bands of our rod-decorated diamond lattice, using the MIT Photonic Bands package[23]. Figure 3a shows the calculated band structure along a rotation about a two-fold axis. The rotation path is illustrated by the dotted red line in Fig. 1d. We found excellent agreement between the observed and calculated gap positions.

To gain insight into these complex spectra, we consider that gaps result from Bragg scattering. A wavevector that resides on the plane defined by a reciprocal lattice vector $\mathbf{G}$ is Bragg-scattered by $\mathbf{G}$. Such a wavevector satisfies the condition $\mathbf{k}\cdot\mathbf{G} = |\mathbf{G}|^2/2$ or equivalently, $|\mathbf{k}| = |\mathbf{G}|/(2\cos\theta)$. To lowest order, the centre frequency of a stop gap is therefore $f_G = (c/\bar{n})|\mathbf{G}|/(4\pi\cos\theta)$, where c is the speed of light in vacuum and $\bar{n}$ is the Bruggeman effective medium index[24]. The dashed curves in Figs 2a and 3b correspond to a $1/\cos(\theta - \theta_o)$ angular dependence consistent with Bragg scattering.

Compared with the diamond structure, the quasicrystal spectrum appears surprisingly less complex. Because the scattering function for a quasicrystal is a dense set of Bragg spots (of zero measure), we might have expected many gaps and zone faces to be intersecting. Instead there appear to be a few well-defined $1/\cos(\theta - \theta_o)$ curves in Fig. 2 and therefore few zone boundaries with sizeable gap formation.

Our method for visualizing the effective Brillouin zone structure is to invert the process by using the gaps to find the zone faces. We locate the points in reciprocal space responsible for the gaps by assuming $|\mathbf{k}(\theta)| \approx \bar{n} f(\theta)/(2\pi c)$. Then, in Fig. 4 we make polar plots of $T(r = f, \theta = \theta)$. For the diamond lattice, data from a rotation about a four-fold axis (dashed line in Fig. 1d) and a two-fold axis (dotted line in Fig. 1d) are shown in Fig. 4b and c, respectively. Figure 4a shows the calculated frequency deviation ($|\delta f| = |(f - (c/\bar{n})|\mathbf{k}|/(2\pi)|$) versus wavevector of the four-fold rotation.

Transmission data for our quasicrystal is shown in Figs 4d and e. The fact that the low-transmission regions correspond to straight lines indicates that the gaps lie on planes. These transmission polar plots, without any further analysis, directly give us the scattering planes and the effective Brillouin zones. In the smallest zone in Fig. 4d and 4e, we see the decagon from the five-fold rotation, and the additional symmetry planes from the orthogonal two-fold rotation, which correspond to the respective cuts of the triacontahedral Brillouin zone shown in Fig. 1c. (The wavevector corresponding to the edge centre of the smallest visible decagon in Fig. 4d is $\tau^2/\sqrt{\tau^2 + 1}$

in units of $2\pi/d$, where d is the rod length.) There are however, several unexpected features: a strong scattering plane along a $45°$ direction, the absence of strong scattering from the '$2_\perp$' plane (dashed line in Fig. 4e; this may be a polarization effect due to the rod decoration of the unit cells), and another strong scattering plane (dash-dotted line in Fig. 4e) not on the triacontahedron. Note that a complete photonic bandgap would result if the dotted blue curves (cuts of a constant-frequency sphere) were contained within the gap of the zone boundary.

We find the following results. First, there is a relatively well-defined effective Brillouin zone, all of whose faces are consistent with the quasicrystal Bragg pattern. Second, the Brillouin zone structure is surprisingly simple despite the fact that a quasicrystal has a dense set of Bragg spots. Third, which is a key result for photonics, the measured Brillouin zone is close to spherical, with the largest difference in gap centre corresponding to 17% (dotted curve in Fig. 2a). Also, our experiments demonstrate that three-dimensional quasicrystals exhibit sizeable stop gaps on reasonably well-defined effective Brillouin zone faces. Hence, despite the quasiperiodicity, much of the intuition built up for conventional crystals may be applied. This experience with crystals suggests that our quasicrystal is far from optimized because it consists solely of thin rods connecting lattice points. A smoother, more spherical, multiply connected, unit-cell decoration with a more equal filled/void ratio would reduce polarization effects and enhance the gap overlap while maintaining the nearly spherical Brillouin zone. Laser tweezers used for particle trapping or two-photon polymerization would allow the construction of a quasicrystalline matrix of dielectric components with a photonic bandgap in the visible spectrum.

1. Joannopoulos, J., Meade, R. D. & Winn, J. Photonic Crystals (Princeton Univ. Press, Princeton, New Jersey, 1995).
2. Yablonovitch, E. Inhibited spontaneous emission in solid-state physics and electronics. Phys. Rev. Lett. 58, 2059–2062 (1987).
3. Forest, J. S. et al. Photonic-bandgap microcavities in optical waveguides. Nature 390, 143–145 (1997).
4. Chan, Y. S., Chan, C. T. & Liu, Z. Y. Photonic band gaps in two dimensional photonic quasicrystals. Phys. Rev. Lett. 80, 956–959 (1998).
5. Dal Negro, L. et al. Light transport through the band-edge states of Fibonacci quasicrystals. Phys. Rev. Lett. 90, 055501 (2003).
6. Cheng, S. S. M., Li, L., Chan, C. T. & Zhang, Z. Q. Defect and transmission properties of two dimensional quasiperiodic photonic band-gap systems. Phys. Rev. B 59, 4091–4099 (1999).
7. Kaliteevski, M. A. et al. Diffraction and transmission of light in low-refractive index Penrose-tiled photonic quasicrystals. J. Phys. Condens. Matter 13, 10459 (2001).
8. Schechtman, D., Blech, I., Gratias, D. & Cahn, J. W. Metallic phase with long-range orientational order and no translational symmetry. Phys. Rev. Lett. 53, 1951–1953 (1984).